Electronic-Spintronic Terahertz Emitter

Chengpeng Yu[1,2] and Shenggang Liu[1,2,*]

[1] *Terahertz Science and Technology Research Center, University of Electronic Science and Technology of China, Chengdu, Sichuan 610054, China*

[2] *Cooperative Innovation Center of Terahertz Science, University of Electronic Science and Technology of China, Chengdu, Sichuan 610054, China*

(Received 18 October 2018; revised manuscript received 10 January 2019; published 21 February 2019)

We present a terahertz (THz) radiation source combining the principles of spintronics and vacuum electronics: the electronic-spintronic THz emitter (E-STE). Different from the traditional laser-driven spintronic THz emitters, E-STE is driven by low-energy electron beams. Working through four steps: the electron-beam excitation of hot electrons, the electron superdiffusion, the inverse spin Hall effect, and the diffraction radiation of the periodic gratings, E-STE is able to emit continuous, monochromatic THz radiation. Detailed theoretical modeling and numerical calculation show that E-STE can cover the whole THz-frequency regime (0.1–10 THz) by modifying the period of the gratings. The electron beam voltage and current are relatively low (voltage $U = 5$ V, 25 V, peak current $I \sim 100$ mA), while the radiation power density and working efficiency are relatively high. (The power density can reach 10^8 W/cm^2, the working efficiency can reach 25%.) This compact and high-power E-STE may contribute to the development of a THz-radiation source integrated on chip.

DOI: 10.1103/PhysRevApplied.11.024055

I. INTRODUCTION

For years, the terahertz (THz) frequency regime (0.1–10 THz) has attracted much attention [1–3]. Located between millimeter waves and infrared on the electromagnetic spectrum, THz radiation possesses the advantages of the two sides. For example, it transmits information much faster than millimeter waves, but at the same time, it can be utilized in long-distance communication in free space [3]; it can be utilized for high-resolution imaging, but at the same time show the inside structures of objects [4]. In addition, THz radiation also exhibits many unique effects that have never been found either in millimeter waves or in infrared. For example, it can cause resonance in many biomolecules (such as proteins and DNA [5]) without damaging the tissues; it can induce nontrivial effects in topological materials (such as topological-edge plasmons in graphene [6]). Therefore, it is promising for use in many areas: space science [7], communication [3,8,9], medicine [10], and so on.

Although the research and development in THz science and technology has been under way for the last 30 years, there are still many problems that remain to be studied further. The most basic and urgent one is the problem of radiation sources. Traditional electronic or photonic radiation sources are not efficient enough to satisfy the growing needs of THz-related fields [5]. To solve this, many new methods and devices have been proposed: graphene surface plasmons polaritons [11,12], quantum cascade lasers [13], laser-induced plasma [2], high-power THz-radiation sources (gyrotrons) [14,15], FeF_2 excited by laser [16], and so on.

At present, spintronic devices, which manipulate both the spin current and charge current induced by the electrons, are proven to be faster, more efficient, and more compact than traditional electronic devices in many fields, especially in the transfer and storage of data [17,18]. In spintronic devices, one of the fundamental effects is the spin Hall effect (SHE). Originating from the spin-orbital coupling of electrons, SHE allows the charge current to generate a transverse spin current. SHE and its inverse effect, the inverse spin Hall effect (ISHE), which allows the generation of charge current from a pure spin current, play key roles in the generation and detection of spin current in spintronic devices [19].

In 2013, based on ISHE, Kampfrath *et al*. theoretically and experimentally discovered the spintronic THz emitter (STE) [20]. In their scheme, a femtosecond laser pulse is irradiated on a bilayer of Fe and Au (or Ru). The laser pulse excites a spin current in the Fe layer, which then enters the Au (or Ru) layer and transforms into a charge current through ISHE. As a result, STE emits a broadband THz pulse.

*liusg@uestc.edu.cn

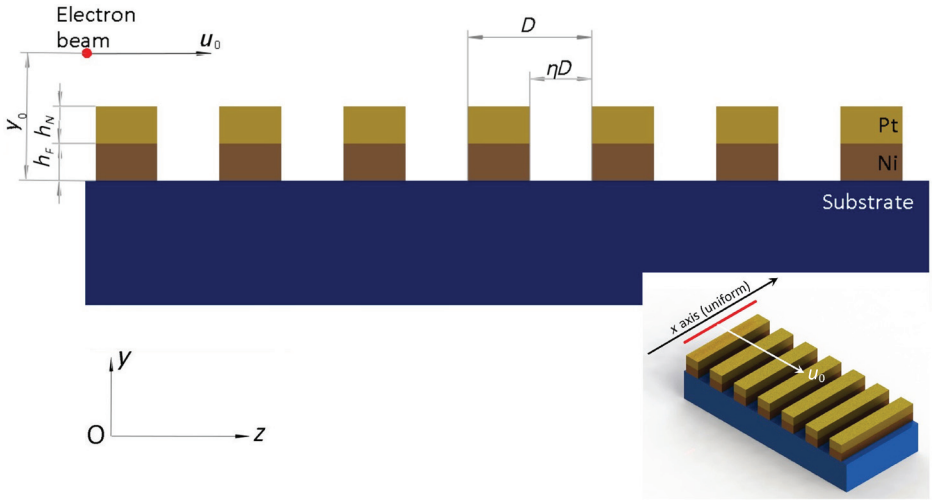

FIG. 1. Configuration of E-STE. Above a dielectric substrate of permittivity $\varepsilon_d = 9$ an electron beam moves uniformly in the z direction with velocity u_0 (corresponding to electron-beam voltage $U = (1/\sqrt{1 - u_0^2/c^2} - 1)mc^2/e$, where m is the rest mass of electron). The distance between the electron beam and the substrate is $y_0 = 20$ nm. Periodic bilayer gratings of Pt and Ni are located on the substrate. The period is D. The gap between each bilayer is ηD with $\eta = 0.5$. The thicknesses of the Pt layer and Ni layer are $h_N = 3$ nm and $h_F = 2$ nm, respectively. A weak static magnetic field $B_0 = 20$ mT is applied in the z direction. The coordinate system is shown on the figure (righthand). The inset shows the 3D plot of E-STE. The whole system is uniform along the x axis.

STE is a promising THz-radiation source, providing an effective way to connect a spin current with traditional electromagnetic radiation [21]. Therefore, STE has been intensively investigated since its discovery. Different materials, such as Pt, Ni, W, and Bi, are utilized in the later proposed STEs, and structural parameters such as the layer thickness are optimized, leading to even stronger field amplitude and wider radiation bandwidth that reaches 8 THz [21–26]. Recently, alternative materials exhibiting completely different ISHE mechanisms have also been discussed, and these materials could replace the nonmagnetic metal (Pt, Au, Ru, etc.) in the bilayer and push the development of STE one step further [27].

However, as far as we know, the later proposed STEs are all driven by femtosecond laser pulses [21–26]. For these kinds of STEs, there might be two restrictions:

(a) The output THz radiation is limited to broadband pulses. On the other hand, continuous, monochromatic THz radiation is important for many applications, especially in the field of communication [8,9].

(b) Even though the bilayer, the key component of STE, is quite small (its thickness is on the nanometer scale [20]), the whole system (including the femtosecond laser source and the corresponding optical components) is still relatively large.

Here, combining the principles of spintronics and vacuum electronics, we theoretically investigate the possibility to drive STE by a low-energy electron beam, whereby the above restrictions can be avoided. An electronic-spintronic terahertz emitter (E-STE) is proposed. E-STE consists of bilayer gratings of Pt and Ni located on a dielectric substrate and an electron beam moving along them, as illustrated in Fig. 1.

We will show that E-STE works through four steps: the electron-beam excitation of hot electrons, the electron superdiffusion, ISHE, and the diffraction radiation of the periodic gratings, and is able to emit continuous, monochromatic THz radiation with a frequency ranging from 0.1 to 10 THz. The required voltage and current of the electron beam are relatively low (voltage $U = 5$ V, 25 V; peak current $I \sim 100$ mA), while the radiation power density and working efficiency are relatively high. (The power density can reach 10^8 W/cm^2, the working efficiency can reach 25%.) Therefore, the investigation of E-STE may contribute to the development of a THz radiation source integrated on chip.

The paper is organized as following: In Sec. II, the emitting mechanism of E-STE is discussed, providing an overall view of how E-STE works. In Sec. III, the theoretical model of E-STE is established to quantitatively describe each step of the emitting mechanism. The important results calculated from the theoretical model are then presented and analyzed in Sec. IV, showing that E-STE does exhibit the properties mentioned in the above paragraph. Finally, the results are summarized in Sec. V.

II. EMITTING MECHANISM

The physical mechanism of the E-STE THz-emitting process consists of four steps:

(a) The electron-beam excitation of hot electrons. When the electron beam moves above a bilayer, it excites an electromagnetic field that varies rapidly in time and space in the bilayer via near-field coupling. At each spatial point, the field signal lasts for less than 100 fs. Because of the locality of interaction mediated by the field, this rapidly varying field is equivalent to the femtosecond laser in an ordinary STE. Therefore, in ferromagnetic metal materials such as Ni, electrons are able to obtain energy from this field [28,29]. (The energy eventually comes from the electron beam through the exchange of near-field photons.) The electrons that obtain energy jump above the Fermi level, becoming hot electrons that can move around freely in the bilayer.

(b) The electron superdiffusion. Due to the superdiffusion mechanism (an electron transport mechanism that lies between ballistic transport and diffusion [30,31]), the excited electrons spread in the Ni layer and eventually enter the Pt layer. In E-STE, a weak static magnetic field $B_0 = 20\,\mathrm{mT}$ is applied to magnetize Ni (see Fig. 1), providing a favorable direction of electron spin (referred as spin-up or $\uparrow$). The average velocities and lifetimes of spin-up electrons are larger than those of an electron of the same energy, but with an opposite spin direction (referred as spin-down or $\downarrow$) [32]. Thus, the superdiffusion brings a macroscopic spin transport from Ni to Pt, referred to as a spin current. (Note that Pt is a nonmagnetic metal material with little velocity or lifetime differences between spin-up and spin-down electrons [32]. Therefore, the electron beam cannot excite a spin current from the Pt layer to the Ni layer.)

(c) ISHE. Due to the strong spin-orbital interaction, the Pt layer is capable of sustaining ISHE at room temperature [33]. ISHE allows the transformation from spin current to the charge current:

$$\vec{J}^{C}(\vec{r},t) = \frac{2e}{\hbar}\theta_{\mathrm{SHE}}\vec{J}^{S}(\vec{r},t) \times \frac{\vec{B}_0(\vec{r},t)}{\left|\vec{B}_0(\vec{r},t)\right|}, \qquad (1)$$

where $\vec{J}^{C}$ is the charge current, $\vec{J}^{S}$ is the spin current, $\theta_{\mathrm{SHE}} = 0.04$ is the spin Hall angle of Pt, $\vec{B}_0/\left|\vec{B}_0\right|$ is the direction of the applied magnetic field [20,33], e is the elementary charge, and $\hbar$ is the reduced Planck constant. Therefore, the spin current injected from the Ni layer gradually transforms into charge current in the Pt layer. The direction of the charge current is determined by the direction of the electron superdiffusion and the direction of the magnetic field.

(d) The diffraction radiation of the periodic gratings. In E-STE, the periodic gratings play a three-fold role:

(1) Unlike the traditional STE, in E-STE, the charge current induced by ISHE (referred to as ISHE current) propagates uniformly with the electron beam. Therefore, unless the Cherenkov condition is fulfilled (which requires the electron-beam voltage to be higher than the regime in which we are interested [34]), the ISHE current cannot spontaneously emit radiation. In E-STE, the gratings are introduced to diffract the ISHE current into radiation.

(2) Since the ISHE current in each bilayer lasts a few hundred femtoseconds [20,21,35] (which is determined by the timescale of the superdiffusion), and because of the periodic distribution of the gratings and the uniformly moving electron beam, the pulses from each bilayer are in-phase. The superposition of these pulses can constitute continuous THz radiation. Thus, the gratings make the radiation continuous.

(3) Because of the in-phase superposition of the pulses from each bilayer, the gratings also make the radiation monochromatic. Since the pulses last for several hundred femtoseconds, there are rich THz components. By tuning the radiation frequency by the period of the gratings, we are able to obtain monochromatic THz radiation.

Therefore, based on periodic gratings, the E-STE is able to emit continuous monochromatic THz radiation. A similar mechanism on the emission of radiation has also been discussed in the context of plasmonics [1,36–39].

III. THEORETICAL MODEL

In this section, the theoretical model of E-STE is established to quantitatively describe each step of the emitting mechanism in Sec. II.

A. Electron-beam excitation of hot electrons

A far as we know, the electron-beam excitation of hot electrons in Ni has not yet been considered [21–26]. Based on the following assumptions, the electron excitation rate can be calculated:

(a) The field of the electron beam consists of different frequency components. These components independently excite electrons in Ni with the same effect as photons of identical frequency.

(b) Affected by the electron-beam field component of the frequency ω, Ni electrons with initial energy $E_F - \hbar\omega < E_i < E_F$ are excited with equal probability, as illustrated in Fig. 2, where E_F is the Fermi energy.

(c) The excitation process only lasts for a short period of time ($\Delta t < 100\,\mathrm{fs}$). Therefore, the thermal effect that is a result of the excitation can be neglected.

(d) The response function (permittivity, conductance, etc.) of Ni in the timescale of a few hundred femtoseconds can be approximated by its long-time response function.

(e) The electron beam is assumed to move uniformly throughout the excitation process. This is because the length of the system is small (The length of each grating

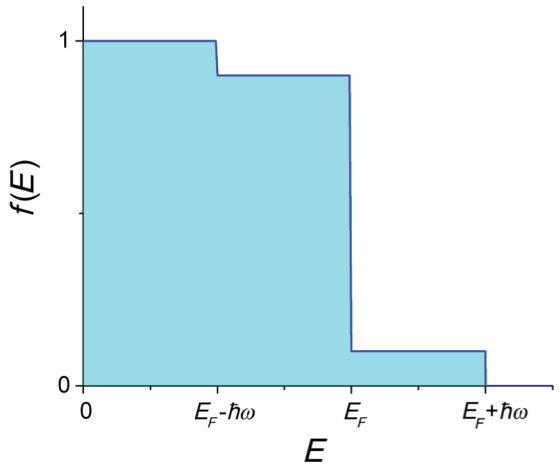

FIG. 2. The distribution of the Ni electrons excited by electron-beam field component of frequency ω. The contributions of other electromagnetic field components are not plotted.

period is smaller than 30 μm, as discussed in Sec. IV C). Each time an electron passes through the system, it only loses a small portion of energy. The same assumption was made in Refs. [1,40,41] concerning beam-wave interaction problems.

Based on assumptions (a)–(e), the electron excitation rate (which is defined as the number density of excited spin $\sigma = \uparrow, \downarrow$ electrons per unit time and energy span, see Appendix A for derivations) is:

$$S^{\text{ext}}(y,z,t,E,\sigma) = p(\sigma)N^{\text{ext}}(y,E)T(y,z,t)u(z), \tag{2}$$

$$N^{\text{ext}}(y,E) = \frac{4\pi}{\hbar^2}\int_{(E-E_F)/\hbar}^{+\infty}\frac{\tilde{\sigma}_F(\omega)}{\omega^2} \times \sum_{i=y,z}|\tilde{E}_i(y,z,\omega)|^2 d\omega, \tag{3}$$

$$T(y,z,t) = \frac{\sum_{i=y,z}J_i(y,z,t)E_i(y,z,t)}{4\pi\sum_{i=y,z}\int_0^{+\infty}\tilde{\sigma}_F(\omega)|\tilde{E}_i(y,z,\omega)|^2 d\omega}, \tag{4}$$

$$u(z) = \begin{cases} 1 & \left(-\frac{\eta}{2}+k\right)D < z < \left(\frac{\eta}{2}+k\right)D, \\ 0 & \text{otherwise}, \end{cases}$$
$$k = \ldots, -1, 0, 1, \ldots, \tag{5}$$

where $p(\sigma)$ is the percentage of the excited spin-up and spin-down electrons, given as $p(\uparrow) = 33.6\%$, $p(\downarrow) = 66.4\%$ [28]; $N^{\text{ext}}(y,E)$ is the total number density of excited Ni electrons per unit energy span; $T(y,z,t)$ is the normalized time evolution function; and $u(z)$ is the profile of the gratings. $\tilde{\sigma}_F(\omega)$ is the frequency-dependent conductivity of Ni, given in Ref. [42]. $E_i(y,z,t)$, $\tilde{E}_i(y,z,\omega)$ are the electric-field signal and spectrum of the electron beam, and $J_i(y,z,t)$ are the currents excited by $E_i(y,z,t)$ in Ni. These three quantities are calculated through Maxwell equations and the boundary conditions given in Appendix A.

B. Electron superdiffusion

Once the electrons are excited, they superdiffuse across the Ni layer. According to the theory of M. Battiato *et al.* [31,35], the number density of spin $\sigma = \uparrow, \downarrow$ electrons per unit energy span ΔE, $n(y,z,t,E,\sigma)$, satisfies

$$\frac{\partial n(y,z,t,E,\sigma)}{\partial t} + \frac{n(y,z,t,E,\sigma)}{\tau(E,\sigma)} = \left(-\frac{\partial}{\partial y}\hat{\phi} + \hat{I}\right)\left[\hat{S}n(y,z,t,E,\sigma) + S^{\text{ext}}(y,z,t,E,\sigma)\right], \tag{6}$$

$$\hat{\phi}f\,(y,z,t,E,\sigma) = \int_{-\infty}^{t} dt_0 \frac{e^{-[(t-t_0)/\tau(R,\sigma)]}}{2v(E,\sigma)(t-t_0)^2} \times \int_{y-v(E,\sigma)(t-t_0)}^{y+v(E,\sigma)(t-t_0)} dy_0 f\,(y_0,z,t_0,E,\sigma) \times (y-y_0), \tag{7}$$

$$\hat{S}f\,(y,z,t,E,\sigma) = \frac{f\,(y,z,t,E,\sigma)}{\tau(E,\sigma)}\theta(E-E_F), \tag{8}$$

where operators $\hat{\phi}$ and $\hat{S}$ correspond to the motions and collisions of the electrons and $\hat{I}$ is the unit operator. $v(E,\sigma)$ and $\tau(E,\sigma)$ are the average velocity and lifetime of the excited electrons, given in Ref. [32], and $\theta(x)$ is the Heaviside function.

The superdiffusion is assumed to be z independent according to Eqs. (6)–(8) (see Theorem 1 in Appendix B for more details). This assumption is fair because: (a) for each bilayer of the gratings, the length in the z direction (>100 nm) is much larger than its thickness (5 nm); (b) to our knowledge, at this length scale, there is no research showing that the surface effect plays an important role in Pt or Ni.

According to the expression $\hat{S}$ [Eq. (8)], the inelastic collisions among electrons and the metal lattice are neglected due to the short timescale of the spin current (several hundred femtoseconds).

To solve Eq. (6), the total reflection boundary condition is applied to the Ni/substrate interface, while the total transmission boundary condition is applied to the Pt/Ni interface.

It is worth noting that Eq. (6) should not be solved analytically through a perturbation approach, because such a result only considers the contribution of the first-generation electrons excited by the electron beam. Since

the electron lifetime is $\tau \sim 10\,\mathrm{fs}$ [32], which is an order of magnitude smaller than the timescale of the spin current, electrons of the later generations excited by collisions play an important role. Therefore, Eq. (6) will be numerically solved through the Euler forward method [35]. The results are presented and discussed in Sec. IV A.

C. ISHE

When the excited eletrons superdiffuse across the Pt/Ni interface, the corresponding spin-current density at the interface is [31,35]

$$\vec{J}^{S}(h_F,z,t) = \frac{\hbar}{2}\vec{e}_y \int_{E_F}^{+\infty} dE[\Phi(h_F,z,t,E,\uparrow) - \Phi(h_F,z,t,E,\downarrow)], \tag{9}$$

$$\Phi(y,z,t,E,\sigma) = \hat{\phi}[\hat{S}n(y,z,t,E,\sigma) + S^{\mathrm{ext}}(y,z,t,E,\sigma)], \tag{10}$$

where h_F is the thickness of the Ni layer, $\Phi(y,z,t,E,\sigma)$ is the flux density of spin $\sigma = \uparrow,\downarrow$ electrons per unit energy span, $\hat{\phi}$ and $\hat{S}$ are defined as Eqs. (7) and (8), and and $\vec{e}_y$ is the unit vector in the y direction (similarly, there are $\vec{e}_x$, $\vec{e}_z$).

Once the spin current enters the Pt layer, it transforms into a charge current due to ISHE and simultaneously decays away. The ISHE current density can be obtained from Eq. (1) and the calculations of Refs. [21,33]. Integrating the ISHE current density over the Pt layer in the y direction, the equivalent ISHE surface current density is obtained as

$$\vec{J}^{C}(z,t) = \theta_{\mathrm{SHE}}\frac{2e}{\hbar}\vec{e}_x J_y^S(h_F,z,t)\lambda_N \times \frac{e^{h_N/\lambda_N} + e^{-(h_N/\lambda_N)} - 2}{e^{h_N/\lambda_N} - e^{-(h_N/\lambda_N)}}, \tag{11}$$

where $\lambda_N = 1.4\,\mathrm{nm}$ is the propagation length for the spin current in Pt [21] and h_N is the thickness of the Pt layer.

D. Diffraction radiation of the periodic gratings

The ISHE current copropagates with the electron beam and is diffracted by the bilayer gratings into radiation in the substrate and free space. Since the ISHE current orients in the x direction [Eq. (11)], and considering that the system is x invariant, $\partial_x \to 0$, it is straight forward to prove $E_z = 0$ from the Maxwell equations. Therefore, the electromagnetic field is TE_z. The electric field in the x direction is expressed as a summation of space harmonics (see Appendix B for derivation):

$$\tilde{E}_x^r(y,z;\omega) = \sum_{n=-\infty}^{+\infty} \frac{-\omega\mu_0\eta\,\mathrm{sinc}\,(\eta n)e^{ik_{zn}z}}{k_{1n}+k_{2n}} \times \left[\frac{1}{2\pi}\int_{-\infty}^{+\infty} d\tau J_x^C(0,\tau)e^{i\omega\tau}\right] \times \begin{cases} e^{ik_{1n}y}, & y>0, \\ e^{-ik_{2n}y}, & y<0, \end{cases} \tag{12}$$

where n is the order of space harmonics, $k_{zn} = \omega/u_0 + 2\pi n/D$, $k_{1n} = \sqrt{\omega^2/c^2 - k_{zn}^2}$, and $k_{2n} = \sqrt{\varepsilon_d\omega^2/c^2 - k_{zn}^2}$ are corresponding wave vectors, D is the period of the bilayer gratings, ηD is the gap between each bilayer, ε_d is the permittivity of the substrate, μ_0 is the vacuum permeability, and c is the speed of light.

From Eq. (12), it is known that the $n=-1$ space harmonic dominates the radiation field. Therefore, the primary frequency of the radiation is (see Appendix B for more details)

$$f_{-1} = \frac{c\beta}{D}\frac{1}{1-\varepsilon_r\beta^2}, \tag{13}$$

where $\beta = u_0/c$ and ε_r is the permittivity in the free space and the substrate. Thus, by modifying the period of the bilayer gratings, the frequency of the output radiation can be changed.

The system presented in Fig. 1 is infinitely large in the x, z direction. A practical system, however, has a finite area. Thus, when an electron beam goes through the system, a specific amount of radiation energy will be emitted. The radiation energy per unit area is (see Appendix C for derivation)

$$w = \mathrm{Re}\sum_{n=-\infty}^{-1}\left[\int_{\omega_1^-}^{\omega_1^+} d\omega k_{1n} + \int_{\omega_2^-}^{\omega_2^+} d\omega k_{2n}\right] \times \left|\frac{1}{2\pi}\int_{-\infty}^{+\infty} d\tau J_x^C(0,\tau)e^{i\omega\tau}\right|^2 \frac{4\pi\omega\mu_0\eta^2\mathrm{sinc}^2(\eta n)}{|k_{1n}+k_{2n}|^2}, \tag{14}$$

where $\omega_1^{\pm} = -2\pi nc\beta/[D(1\mp\beta)]$ are the upper and lower bounds of the radiation frequency in the free space and $\omega_2^{\pm} = -2\pi nc\beta/[D(1\mp\sqrt{\varepsilon_d}\beta)]$ are the upper and lower bounds of the radiation frequency in the substrate.

Considering an electron gun that emits electron beams periodically into E-STE with a repetition rate f_r, the radiation power density is defined as $P = wf_r$.

The working efficiency of the system, on the other hand, is defined as the ratio between the radiation energy per unit area, w, and the work done per unit area by the electron

beam, W: $\xi = w/W$. Making use of the Parseval theorem, W is given as

$$W = 4\pi(1-\eta)\int_0^{+\infty}[h_F\tilde{\sigma}_F(\omega) + h_N\tilde{\sigma}_N(\omega)] \times \sum_{i=y,z}|\tilde{E}_i(0,z,\omega)|^2 d\omega, \quad (15)$$

where $\tilde{\sigma}_N(\omega)$ is the frequency-dependent conductivity of Pt as given in Ref. [42].

IV. RESULTS AND ANALYSIS OF CALCULATIONS

Based on the theoretical mode in Sec. III and calculations, the properties of E-STE are obtained and analyzed. Some important results are presented below.

A. Motion of the electrons with different energy and spin

Solving Eqs. (6)–(8) numerically, the motions of the electrons with different energies and spins are calculated. Taking the voltage of the electron beam to be $U = 5$ V, the space-time distribution of $n(y,z,t,E,\sigma)$in a bilayer is plotted in Fig. 3.

The results in Fig. 3 indicate:

(a) When excited by an electron beam, the relaxation time of the hot electrons is several hundred femtoseconds [Figs. 3(c)–3(f)], which corresponds to the THz-frequency regime.

(b) When the electron energy is low, the superdiffusion is suppressed due to the low electron average velocity [Figs. 4(a) and 4(b)]. Therefore, the spin current is primarily excited by the electron-beam field components in or above the optical frequency (frequency $f \sim 100$ THz, which can excite Ni electrons to $E_f + 0.4$ eV).

(c) With the same energy, the relaxation time of the spin-up electrons is remarkably smaller than that of the spin-down electrons. The superdiffusion of spin-up electrons is much stronger. Thus, the macroscopic spin current is spin-up.

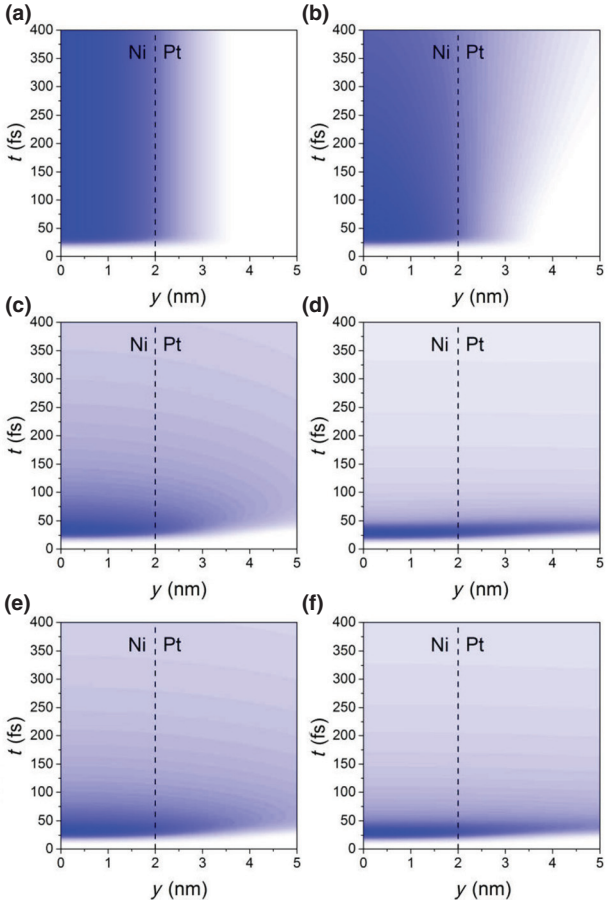

FIG. 3. The space-time distribution of $n(y,z,t,E,\sigma)$ in a bilayer. The energy and spin of the electrons are: (a) $E = 0.01$ eV, $\sigma = \downarrow$, (b) $E = 0.01$ eV, $\sigma = \uparrow$, (c) $E = 0.5$ eV, $\sigma = \downarrow$, (d) $E = 0.5$ V, $\sigma = \uparrow$, (e) $E = 2$ eV, $\sigma = \downarrow$, and (f) $E = 2$ eV, $\sigma = \uparrow$, respectively. (The Fermi energy E_F is chosen as the reference energy.) The voltage of the electron beam $U = 5$ V and the z coordinates are fixed to be $z = 0$. (According to Theorem 1 in Appendix B, as long as $n(y,0,t,E,\sigma)$ is known, we can deduce $n(y,z,t,E,\sigma)$ at any z). The Pt layer and Ni layer are separated by the dashed line on each figure.

B. Relation between the ISHE current and the electron-beam voltage

According to Eq. (11), in the bilayers, the ISHE current is in the x direction. The surface current density with different electron-beam voltages is shown as Fig. 4(a). The corresponding frequency spectrum is plotted as well in Fig. 4(b).

The results in Fig. 4 indicate:

(a) The ISHE current has rich THz components [Fig. 4(b)]. Therefore, modifying the period of the bilayer gratings with respect to Eq. (13), E-STE can output the THz radiation of a given frequency.

(b) The amplitude of the ISHE surface current density decreases as the electron-beam voltage increases and nearly vanishes when $U = 50$ V. This is because if an electron beam interacts with a system through the near field, as the electron beam moves faster, the exchange of energy will become less efficient [41]. Therefore, a high-voltage electron beam cannot efficiently excite hot electrons in Ni. Of course, to preserve the assumption that the electron beam moves uniformly (as stated in Sec. I), the voltage of the electron beam cannot be chosen to be arbitrarily low, otherwise the length of the system will be seriously limited.

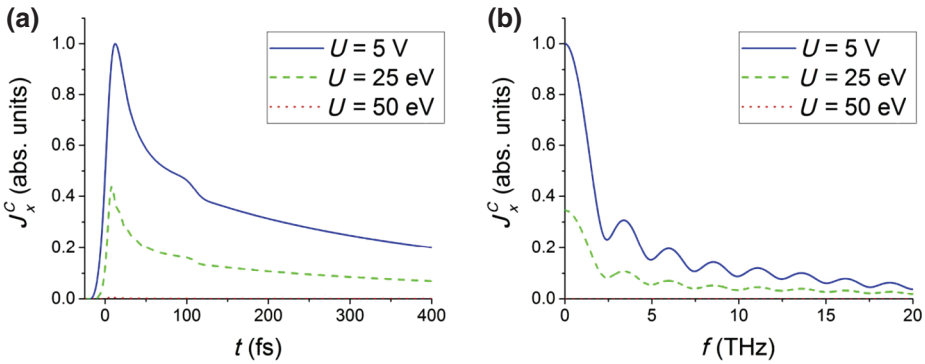

FIG. 4. The ISHE surface current density J_x^C in a bilayer excited by an electron beam of different voltage. (a) Time domain signal, (b) frequency spectrum. The z coordinates are fixed to be $z = 0$. All data are normalized by the peak value of the $U = 5$ V curve.

C. Spectrum and distribution of the radiation field

As stated in Sec. IV B, THz radiation of a different frequency can be emitted by modifying the period of the gratings. From Eq. (13), the relation between the primary radiation frequency f_0 and the gratings period D is estimated: for electron-beam voltage $U = 5$ V, when $f_0 = 0.1$, 0.5, 1 ,2, 3, 10 THz, $D = 13.25$, 2.65, 1.33, 0.663, 0.442, 0.133 μm; for an electron-beam voltage $U = 25$ V, when $f_0 = 0.1$, 0.5, 1 ,2, 3, 10 THz, $D = 29.66$, 5.93, 2.97, 1.48, 0.989, 0.297 μm.

With the primary radiation frequency $f_0 = 0.5$, 1, 2, 3 THz and the electron-beam voltage $U = 5$ V, 25 V, the spectrum of the radiation electric field E_x^r is calculated through Eq. (12), as shown in Fig. 5.

On the other hand, for frequency $f_0 = 1, 3$ THz and electron-beam voltage $U = 5$ V or 25 V, the distribution of E_x^r at $t = 0$ is shown in Fig. 6.

The results in Figs. 5 and 6 show:

(a) The radiation is continuous and monochromatic.

(b) By modifying the period of the bilayers in a reasonable range (13.25–0.133 μm, 29.66–0.297 μm), E-STE is able to emit radiation covering the whole THz frequency regime (0.1–10 THz).

(c) Apart from the radiation of frequency f_0, E-STE also emits radiation from higher-order space harmonics. Both types of radiation are fairly monochromatic, especially at the electron-beam voltage $U = 5$ V.

(d) The TE_z radiation wave is emitted into the substrate and free space at the same time. The field in the substrate is stronger due to the higher refraction index.

(e) The radiation wave is distributed over a large angle. This angle is mainly determined by the primary radiation frequency f_0, and is not significantly affected by the

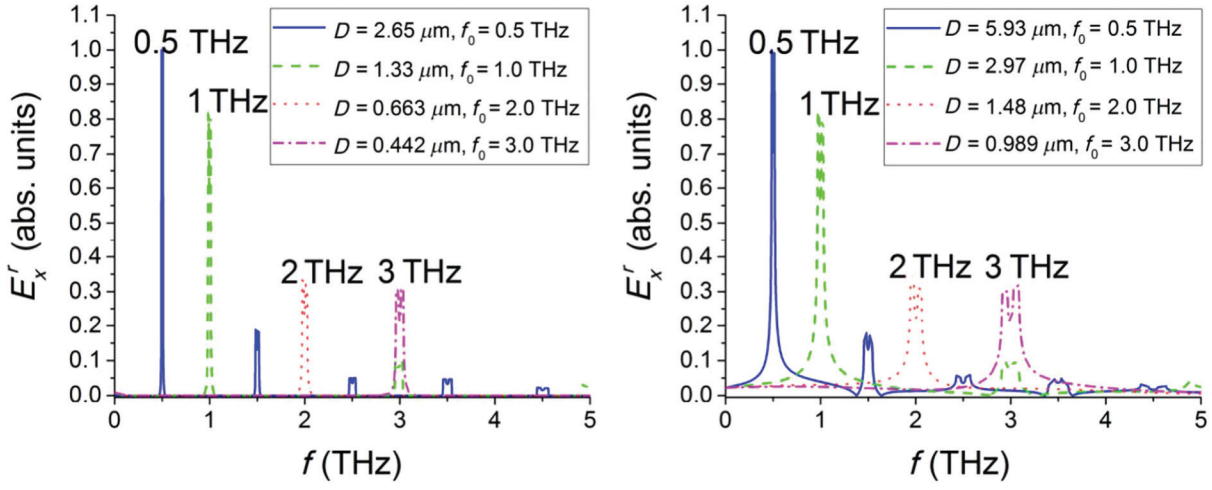

FIG. 5. The spectrum of the radiation electric field E_x^r with different primary radiation frequencies f_0. The electron beam voltage is: (a) $U = 5$ V and (b) $U = 25$ V, respectively. The spectrum is measured at $z = 0$, $y = -10$D. For each curve, the spectrum peak location is labeled. All data are normalized by the peak value of the $f_0 = 0.5$ THz spectrum.

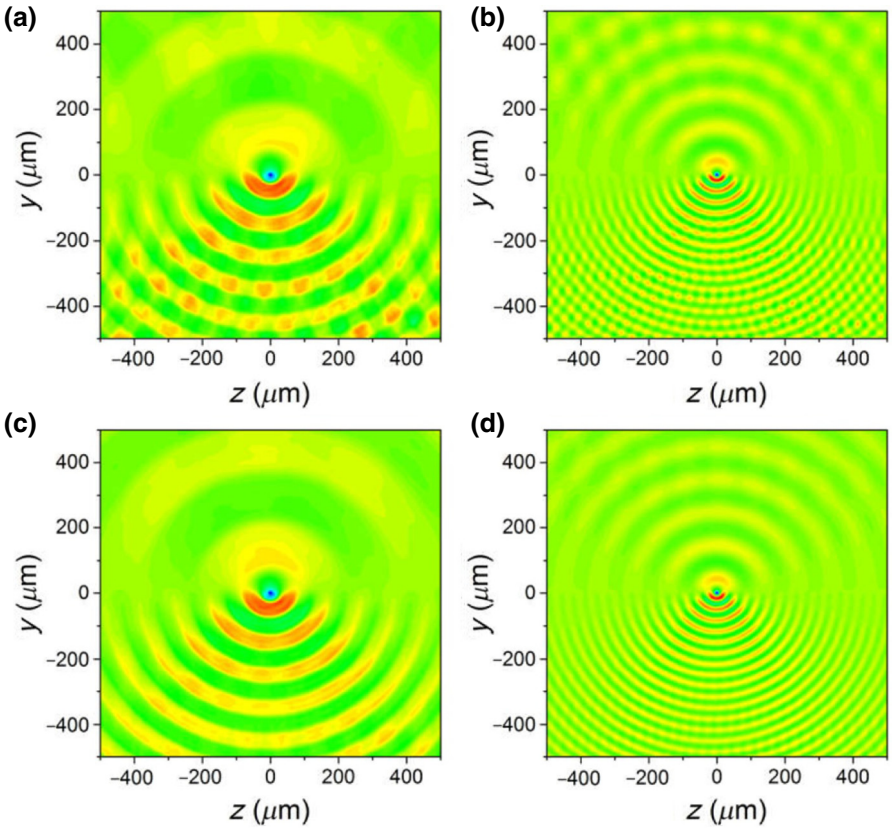

FIG. 6. The distribution of E_x^r at $t = 0$. The electron beam is located near the origin. The electron beam voltages and the primary radiation frequencies are: (a) $U = 5$ V, $f_0 = 1$ THz, (b) $U = 5$ V, $f_0 = 3$ THz, (c) $U = 25$ V, $f_0 = 1$ THz, and (d) $U = 25$ V, $f_0 = 3$ THz, respectively.

electron beam voltage U or the gratings period D. This would make collection of the radiation easier.

D. Power density and efficiency

Considering an electron gun that emits electron beams with a repetition rate $f_r = 10$ MHz and peak current $I \sim 100$ mA (which is quite experimentally achievable [43, 44]), the radiation power density P defined in Sec. III D is calculated at different I, shown as Fig. 7.

The results in Fig. 7 show:

(a) E-STE has a relatively high radiation power density. Excited by an electron beam with repetition rate $f_r = 10$ MHz, the radiation power density P can reach as high as 10^8 W/cm^2. This can help reduce the size of the E-STE-based THz systems.

(b) The radiation power first goes up and then goes down with the increase of the primary radiation frequency f_0. When $0.5\,\text{THz} < f_0 < 2\,\text{THz}$, the largest values are obtained. This is the optimized working frequency of E-STE.

Once the peak current I of the electron beam is known, the working efficiency ξ defined in Sec. III D can also be estimated. The results show:

(a) The working efficiency ξ increases with the peak current I in the same manner as the radiation power density P.

(b) E-STE has a relatively high working efficiency. With a reasonable electron-beam peak current ($I \sim 100$ mA) and radiation frequency ($f_0 \sim 1$ THz), the theoretical value of the working efficiency ξ can reach and even exceed 25%.

(c) The working efficiency ξ also reaches the largest values when $0.5\,\text{THz} < f_0 < 2\,\text{THz}$.

E. Comparing E-STE and Laser-Driven Spintronic THz Emitters

As stated in Sec. I, presently, Laser Driven Spintronic THz Emitters (LSTE) are studied most intensively. Therefore, it is necessary to compare the E-STE proposed here with LSTE.

Just as expected in Sec. I, E-STE has the following advantages over LSTE:

(a) To drive LSTE, femtosecond lasers are needed [20–26], while E-STE only needs low-energy electron beams ($U = 5$, 25 V). Having studied vacuum electronics for so many years [40–45], the techniques to generate low-energy electron beams are quite mature and the power is also significantly high. Therefore, based on E-STE, a new

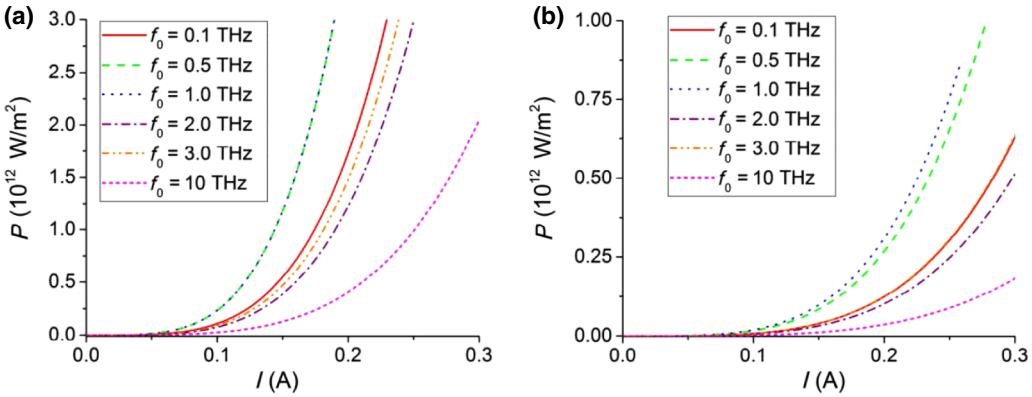

FIG. 7. The radiation power density P at different electron-beam peak currents I and primary radiation frequencies f_0. The voltage of the electron is: (a) $U = 5$ V and (b) $U = 25$ V. The electron-beam repetition rate is $f_r = 10$ MHz.

approach can be found to realize compact, high-power, and practical THz systems.

(b) LSTE can only emit broadband THz pulses. The central frequency is fixed by the materials that build the bilayer [20–23], while E-STE can emit continuous, monochromatic THz radiation with a frequency regime from 0.1 to 10 THz. Thus, having these characteristics makes E-STE possess wide applications [8,9].

Compared with LSTE, E-STE can be further improved with the following aspect: In LSTE, the energy of the hot electrons can be controlled by the frequency of the input laser, therefore, achieving an optimized value for the generation of the spin current; while in E-STE, part of the hot electrons excited by the electron beam has low energy and cannot effectively generate a spin current (Sec. IV A). Thus, E-STE's current efficiency is lower than that of LSTE. The latter can reach 10%–25% in experiments [21].

However, considering that low-energy electron guns are very efficient [43,44], E-STE-based THz systems may actually possess a higher overall working efficiency than that of LSTE-based ones.

V. CONCLUSION

To summarize, by combining the principles of spintronics and vacuum electronics, E-STE is presented in this paper. As an alternative THz-radiation source, E-STE utilizes low-energy electron beams instead of lasers. It works through four steps: the electron-beam excitation of hot electrons, the electron superdiffusion, ISHE, and the diffraction radiation of the periodic gratings.

Theoretical and numerical investigations show that E-STE has the following advantages:

(a) The radiation is continuous and monochromatic.

(b) The voltage and current of the electron beam are relatively low (voltage $U = 5$ V, 25 V; peak current $I \sim 100$ mA), while the radiation power density and working efficiency are relatively high. (For favorable parameters, the power density can reach as high as 10^8 W/cm^2 and the working efficiency can reach 25%.)

(c) The radiation frequency can cover the whole THz regime (0.1–10 THz) by modifying the period of the gratings.

To conclude, the E-STE presented and investigated here is compact and powerful. Therefore, E-STE may contribute to the development of a THz-radiation source that can be integrated on chip.

ACKNOWLEDGMENTS

This work is supported by the National Basic Research Program (Grant No. 2014CB339801), the National Natural Science Foundation of China (NSFC) (Grants No. 61231005 and No. 61701084) and Sichuan Sci-Tech Support Program (Grant No. 2011GZ0221).

APPENDIX A: DERIVATION OF THE ELECTRON-BEAM EXCITATION OF HOT ELECTRONS

The electron beam with velocity u_0 introduces charge and current density into the system:

$$\rho(y,z,t) = q\delta(z - u_0 t)\delta(y - y_0), \tag{A1}$$

$$\vec{J}(y,z,t) = \vec{e}_z q u_0 \delta(z - u_0 t)\delta(y - y_0), \tag{A2}$$

where q is the charge of each electron beam, $\delta(x)$ is the Dirac function, and y_0 is the distance between the electron beam and the substrate, as shown in Fig. 1.

Considering that the thickness of the bilayers is small, through Maxwell equations and the boundary conditions, the field excited by the electron beam can be obtained. The

electric field spectrum in the Ni layer is

$$\tilde{E}_z(y,z;\omega) = \frac{\mu_0 q\omega}{4\pi k_1}\left(\frac{1}{\beta^2}-1\right) \times \left(\frac{1-(\varepsilon_d k_1/k_2)}{1+(\varepsilon_d k_1/k_2)}e^{ik_1 y}+e^{-ik_1 y}\right)e^{ik_1 y_0}e^{ik_z z}, \tag{A3}$$

$$\tilde{E}_y(y,z;\omega) = \frac{\mu_0 q\omega}{4\pi k_1}\left(\frac{1}{\beta^2}-1\right) \times \left(-\frac{1-(\varepsilon_d k_1/k_2)}{1+(\varepsilon_d k_1/k_2)}e^{ik_1 y}+e^{-ik_1 y}\right) \times \frac{k_z}{k_1}e^{ik_1 y_0}e^{ik_z z}, \tag{A4}$$

where $k_z = \omega/u_0$, $k_1 = \sqrt{\omega^2/c^2 - k_z^2}$, and $k_2 = \sqrt{\varepsilon_d\omega^2/c^2 - k_z^2}$. The spectrum of the current density excited by the electron-beam field in Ni is $\tilde{\vec{J}}(y,z,\omega) = \tilde{\sigma}_F(\omega)\tilde{\vec{E}}(y,z,\omega)$. The time domain signals $\vec{E}(y,z,t)$ and $\vec{J}(y,z,t)$ can be calculated easily through Fourier transformation.

The density of the work done by the electron beam to Ni is estimated as

$$W(y,z) = \sum_{i=y,z}\int_{-\infty}^{+\infty} J_i(y,z,t)E_i(y,z,t)dt. \tag{A5}$$

Since the response function of Ni can be approximated by its long-time response function and according to Parseval theorem, Eq. (A5) is simplified as

$$W(y,z) = \int_0^{+\infty}\tilde{W}(y,z,\omega)d\omega, \tag{A6}$$

$$\tilde{W}(y,z,\omega) = 4\pi\tilde{\sigma}_F(\omega)\sum_{i=y,z}\left|\tilde{E}_i(y,z,\omega)\right|^2. \tag{A7}$$

Therefore, $\tilde{W}(y,z,\omega)$ is the density of the work spectrum done by the electron beam to Ni.

The effect of each $\tilde{W}(y,z,\omega)$ is just like that of the photons of frequency ω. Because Ni electrons with initial energy $E_F - \hbar\omega < E_i < E_F$ are excited with equal probability, and the thermal effect that comes with the excitation can be neglected, this causes Ni electrons of amount $W(y,z,\omega)/(\hbar\omega)$ in energy range $E_F - \hbar\omega < E_i < E_F$ to jump to energy levels $E_i + \hbar\omega$, and the transition probability distribution is $P(E_i) = 1/\hbar\omega$ and $E_F - \hbar\omega < E_i < E_F$. Thus, the total number density of excited Ni electrons per unit energy span is

$$N^{\text{ext}}(y,z,E) = \int_{(E-E_F)/\hbar}^{+\infty}\frac{\tilde{W}(y,z,\omega)}{\hbar\omega}\frac{1}{\hbar\omega}d\omega. \tag{A8}$$

Of course, the number density of excited electrons in Eq. (A8) is only achieved when the electron beam completely goes through the system. The electron excitation rate is proportional to the instantaneous power done by the electron beam to the Ni layer $\sum_{i=y,z}J_i(y,z,t)E_i(y,z,t)$, which is normalized as $T(y,z,t)$ in Eq. (4).

The excited electrons are either spin-up or spin-down. The percentage of these two types of electrons, $p(\uparrow), p(\downarrow)$, are given in Sec. III A.

The profile of the bilayer gratings shall be considered as well, introducing an extra factor $u(z)$, which is given as Eq. (5).

Considering all the aspects above, the electron excitation rate is obtained by multiplying $N^{\text{ext}}(y,z,E)$, $T(y,z,t)$, $p(\sigma)$, and $u(z)$ together, as shown in Eq. (2).

APPENDIX B: DERIVATION OF THE RADIATION FIELD

Through Maxwell equations and the boundary conditions, the radiation field can be obtained from the ISHE surface current density $\vec{J}^{C}(z,t)$. Since the ISHE current orients in the x direction [Eq. (11)], the electromagnetic field is TE_z. The electric field in the x direction is

$$\tilde{E}_x^r(y,z;\omega) = \frac{1}{2\pi}\int_{-\infty}^{+\infty}dk_z\left[-\frac{\omega\mu_0}{k_1+k_2} \times \left[\frac{1}{2\pi}\int_{-\infty}^{+\infty}dze^{-ik_z z}\int_{-\infty}^{+\infty}dte^{i\omega t}J_x{}^{C}(z,t)\right] \times e^{ik_z z}\begin{cases}e^{ik_1 y} & y>0\\ e^{-ik_2 y} & y<0\end{cases}\right]. \tag{B1}$$

Equation (B1) can be simplified further with the following theorem.

Theorem 1: $S^{ext}(y,z,t,E,\sigma)$, $n(y,z,t,E,\sigma)$, $\vec{J}^{S}(h_F,z,t)$, and $\vec{J}^{C}(z,t)$ have the following property:

$$f(z,t) = f\left(0,t-\frac{z}{u_0}\right)u(z). \tag{B2}$$

Proof: Because the electron beam moves uniformly across the system, the electrical field $\vec{E}(y,z,t)$ and corresponding current in Ni $\vec{J}(y,z,t)$ satisfy $f(z,t) = f(0,t-z/u_0)$, as shown in Eqs. (A3) and (A4). Thus, $T(y,z,t)$ in Eq. (4) satisfies $f(z,t) = f(0,t-z/u_0)$. On the other hand, $p(\sigma)$ and $N^{\text{ext}}(y,E)$ in Eq. (3) are z invariant.

Therefore, according to Eq. (2), $S^{\text{ext}}(y,z,t,E,\sigma)$ follows relation (B2).

$n(y,z,t,E,\sigma)$ also follows relation (B2). To prove this, two extra properties of operator $\hat{\phi}$ are needed:

$$[\hat{\phi}f\,](y,z,t-t_1,E,\sigma) = \hat{\phi}[f\,(y,z,t-t_1,E,\sigma)], \tag{B3}$$

$$[\hat{\phi}S^{\text{ext}}](y,z,t,E,\sigma) = [\hat{\phi}S^{\text{ext}}]\left(y,0,t-\frac{z}{u_0},E,\sigma\right), \quad u(z)\neq 0 \tag{B4}$$

These properties can be easily proved through the definition of $\hat{\phi}$ [Eq. (7)]. When $u(z)\neq 0$, substituting $z=0$ and $t=\hat{t}-z/u_0$ into Eq. (6) and making use of properties (B3) and (B4), it is proved that

$$\begin{aligned}&\frac{\partial n(y,0,\hat{t}-(z/u_0),E,\sigma)}{\partial \hat{t}} + \frac{n(y,0,\hat{t}-(z/u_0),E,\sigma)}{\tau(E,\sigma)} \\ &-\left(-\frac{\partial}{\partial y}\hat{\phi}_{\hat{t}}+\hat{I}\right)\left[\frac{n(y,0,\hat{t}-(z/u_0),E,\sigma)}{\tau(E,\sigma)}\right] \\ &=\left[\left(-\frac{\partial}{\partial y}\hat{\phi}+\hat{I}\right)S^{\text{ext}}\right](y,z,\hat{t},E,\sigma)\,,\end{aligned} \tag{B5}$$

where operator $\hat{\phi}_{\hat{t}}$ is obtained by replacing t in $\hat{\phi}$ [Eq. (7)] with $\hat{t}$. Thus, $n(y,0,\hat{t}-z/u_0,E,\sigma)$ follows the same differential equation as $n(y,z,\hat{t},E,\sigma)$. Considering the uniqueness of the solution of Eq. (6), it can be further concluded that $n(y,0,\hat{t}-z/u_0,E,\sigma)=n(y,z,\hat{t},E,\sigma)$. When $u(z)=0$, obviously $n(y,z,\hat{t},E,\sigma)=0$. Therefore, $n(y,z,\hat{t},E,\sigma)=n(y,0,\hat{t}-z/u_0,E,\sigma)u(z)$. This finishes the proof that $n(y,z,t,E,\sigma)$ also follows relation (B2).

Since $S^{\text{ext}}(y,z,t,E,\sigma)$ and $n(y,z,t,E,\sigma)$ all follow relation (B2), from Eq. (10) and properties (B3) and (B4), it is proved that $\Phi(y,z,t,E,\sigma)$ follows relation (B2) as well. Finally, through Eqs. (9) and (11), $\vec{J}^{\,S}(h_F,z,t)$ and $\vec{J}^{\,C}(z,t)$ also satisfy relation (B2). Therefore, the proof of Theorem 1 is finished.

From Theorem 1, $J_x^C(z,t)$ can be re-expressed as $J_x^C(0,t-z/u_0)u(z)$. Substituting this expression into Eq. (B1), the radiation electric field [Eq. (12)] is obtained.

The electric field in Eq. (12) consists of different space harmonics numbered as $n=\ldots,-1,0,1,\ldots$. A space harmonic can radiate out into the substrate (free space) only if $\text{Im}\,k_{2n}=0$ ($\text{Im}\,k_{1n}=0$). This implies the frequency of the radiative space harmonic satisfies $-nc\beta/[D(1+\sqrt{\varepsilon_r}\beta)] < f < -nc\beta/[D(1-\sqrt{\varepsilon_r}\beta)]$ (where $\varepsilon_r=\varepsilon_d$ for the substrate and $\varepsilon_r=1$ for the free space). Therefore, only $n<0$ harmonics can emit radiation and the central frequency of the radiation is $f_n=-nc\beta/[D(1-\varepsilon_r\beta^2)]$. Since $n=-1$ space harmonic dominates the radiation, the primary frequency of the radiation is given as Eq. (13).

APPENDIX C: DERIVATION OF THE RADIATION ENERGY

Consider a double-plane $y=\pm r$ ($r\gg 0$) that surrounds the whole system. The energy that flows out of the double plane is the radiation energy of the system.

On each point of the double plane, the flowed-out energy density

$$w(y,z)=\int_{-\infty}^{+\infty}\frac{y}{|y|}\vec{S}^{\,r}(y,z,t)\cdot\vec{e}_y dt, \tag{C1}$$

where $\vec{S}^{\,r}(y,z,t)$ is the Poynting vector of the radiation field. Since the radiation field is TE_z, $\vec{S}^{\,r}(y,z,t)\cdot\vec{e}_y = -E_x^r(y,z,t)H_z^r(y,z,t)$.

According to the Parseval theorem and Maxwell equations, $w(y,z)$ is expressed in the frequency domain as

$$w(y,z)=\frac{y}{|y|}4\pi\,\text{Re}\int_0^{+\infty}d\omega\frac{1}{i\mu_0\omega}\frac{\partial\tilde{E}_x^r(y,z,\omega)}{\partial y}\tilde{E}_x^{r*}(y,z,\omega). \tag{C2}$$

Substituting the expression of $E_x^r(y,z,\omega)$ from Eq. (12) into Eq. (C2), $w(y,z)$ is obtained:

$$\begin{aligned}w(y,z)=\text{Re}\int_0^{+\infty}d\omega&\left|\frac{1}{2\pi}\int_{-\infty}^{+\infty}d\tau J_x{}^C(0,\tau)e^{i\omega\tau}\right|^2 \\ &\times\sum_{n=-\infty}^{+\infty}\sum_{\bar{n}=-\infty}^{+\infty}\frac{-4\pi i\omega\mu_0\eta^2\text{sinc}^2(\eta n)e^{i\frac{2\pi}{D}(\bar{n}-n)z}}{(k_{1n}+k_{2n})^*(k_{1\bar{n}}+k_{2\bar{n}})} \\ &\times\begin{cases}ik_{1\bar{n}}e^{i(k_{1\bar{n}}-k_{1n}^*)y}, & y>0,\\ ik_{2\bar{n}}e^{-i(k_{2\bar{n}}-k_{2n}^*)y}, & y<0.\end{cases}\end{aligned} \tag{C3}$$

$w(y,z)$ oscillates rapidly along the z direction and the average flowed-out energy density is

$$\begin{aligned}w(y)=\text{Re}\sum_{n=-\infty}^{+\infty}\int_0^{+\infty}d\omega&\left|\frac{1}{2\pi}\int_{-\infty}^{+\infty}d\tau J_x^C(0,\tau)e^{i\omega\tau}\right|^2 \\ &\times\frac{-4\pi i\omega\mu_0\eta^2\text{sinc}^2(\eta n)}{|k_{1n}+k_{2n}|^2} \\ &\times\begin{cases}ik_{1n}e^{-2\text{Im}k_{1n}y}, & y>0,\\ ik_{2n}e^{2\text{Im}k_{2n}y}, & y<0.\end{cases}\end{aligned} \tag{C4}$$

In practical situations, only the energy flow in the far field is important. Therefore, $y=|r|(r\gg 0)$ should be considered to further simplify the equation into a y free form. In doing so, all the space harmonics that are evanescent in the y direction should be omitted. This introduces four quantities: $\omega_1^{\pm}$ are the upper and lower bounds of $\text{Im}\,k_{1n}=0$ and $\omega_2^{\pm}$ are the upper and lower bounds of $\text{Im}\,k_{2n}=0$.

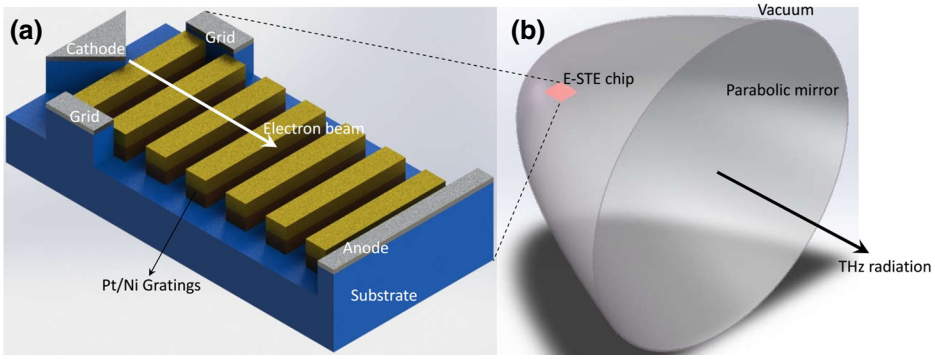

FIG. 8. One of the possible designs of the full device. (a) E-STE is integrated on chip with a planar electron emitter consisting of a cathode, a grid, and an anode. By applying voltage, the electron emitter emits free electrons from the tip of the cathode to the anode. The electron-beam emitter is technically achievable, see Ref. [40]. (b) The whole E-STE chip is placed on the focus of a parabolic mirror to collect the emitted THz radiation. The whole system is in a vacuum chamber.

Their definitions are given in Sec. III D. Making use of $\omega_1^{\pm}$ and $\omega_2^{\pm}$, the energy flow can be simplified as

$$w(y)=\begin{cases}\mathrm{Re}\displaystyle\sum_{n=-\infty}^{-1}\int_{\omega_1^-}^{\omega_2^+}d\omega\left|\frac{1}{2\pi}\int_{-\infty}^{+\infty}d\tau J_x^C(0,\tau)e^{i\omega\tau}\right|^2 \\ \quad\times\dfrac{4\pi k_{1n}\omega\mu_0\eta^2\mathrm{sinc}^2(\eta n)}{|k_{1n}+k_{2n}|^2}, & y>0, \\ \mathrm{Re}\displaystyle\sum_{n=-\infty}^{-1}\int_{\omega_2^-}^{\omega_2^+}d\omega\left|\frac{1}{2\pi}\int_{-\infty}^{+\infty}d\tau J_x^C(0,\tau)e^{i\omega\tau}\right|^2 \\ \quad\times\dfrac{4\pi k_{2n}\omega\mu_0\eta^2\mathrm{sinc}^2(\eta n)}{|k_{1n}+k_{2n}|^2}, & y<0.\end{cases} \tag{C5}$$

The radiation energy per unit area is obtained by summing up the flowed-out energy of planes $y=\pm r$ and $w=w(r)+w(-r)$. The result is shown in Eq. (14).

APPENDIX D: ONE POSSIBLE DESIGN OF THE EXPERIMENTAL IMPLEMENTATION OF E-STE

One of the possible designs of the full device is plotted in Fig. 8. That figure includes the vacuum space, the electron beam source, and the THz-radiation collection system.

Note that although the electron beam in Fig. 8 is not x invariant as assumed in our theory, it can be designed to cover a large part of the area of the gratings. In this situation, our theory can predict the output of the device. In addition, Fig. 8 is not the only possible configuration. For example, instead of the planar electron emitter, a sheet electron-beam gun can also be utilized [46], then the brightness of the obtained THz radiation can be improved.

[1] S. Liu, C. Zhang, M. Hu, X. Chen, P. Zhang, S. Gong, T. Zhao, and R. Zhong, Coherent and tunable terahertz radiation from graphene surface plasmon polaritons excited by an electron beam, Appl. Phys. Lett. **104**, 201104 (2014).

[2] V. A. Andreeva, O. G. Kosareva, N. A. Panov, D. E. Shipilo, P. M. Solyankin, M. N. Esaulkov, P. González de Alaiza Martínez, A. P. Shkurinov, V. A. Makarov, L. Bergé, and S. L. Chin, Ultrabroad Terahertz Spectrum Generation From an Air-Based Filament Plasma, Phys. Rev. Lett. **116**, 063902 (2016).

[3] T. Nagatsuma, G. Ducournau, and C. C. Renaud, Advances in terahertz communications accelerated by photonics, Nat. Photo. **10**, 371 (2016).

[4] K. Ahi, S. Shahbazmohamadi, and N. Asadizanjani, Quality control and authentication of packaged integrated circuits using enhanced-spatial-resolution terahertz time-domain spectroscopy and imaging, Opt. Laser Eng. **104**, 274 (2018).

[5] S. S. Dhillon *et al.*, The 2017 terahertz science and technology roadmap, J. Phys. D: Appl. Phys. **50**, 043001 (2017).

[6] D. Jin, T. Christensen, M. Soljačić, N. X. Fang, L. Lu, and X. Zhang, Infrared Topological Plasmons in Graphene, Phys. Rev. Lett. **118**, 245301 (2017).

[7] P. H. Siegel, THz instruments for space, IEEE Trans. Antenn. Propag. **55**, 2957 (2007).

[8] S. Preu, G. H. Döhler, S. Malzer, L. J. Wang, and A. C. Gossard, Tunable, continuous-wave terahertz photomixer sources and applications, J. Appl. Phys. **109**, 061301 (2011).

[9] S. W. Huang, J. Yang, S. H. Yang, M. Yu, D.-L. Kwong, T. Zelevinsky, M. Jarrahi, and C. W. Wong, Globally Stable Microresonator Turing Pattern Formation for Coherent High-Power THz Radiation On-Chip, Phys. Rev. X **7**, 041002 (2017).

[10] X. Yang, X. Zhao, K. Yang, Y. Liu, Y. Liu, W. Fu, and Y. Luo, Biomedical applications of terahertz spectroscopy and imaging, Trends Biotechnol. **34**, 810 (2016).

[11] T. Zhao, M. Hu, R. Zhong, S. Gong, C. Zhang, and S. Liu, Cherenkov terahertz radiation from graphene surface plasmon polaritons excited by an electron beam, Appl. Phys. Lett. **110**, 231102 (2017).

[12] Y. Liu, R. Zhong, H. Ding, and S. Liu, Graphene loaded double ridge plasmon terahertz waveguide, Eur. Phys. J. D **71**, 83 (2017).

[13] A. Albo, Y. V. Flores, Q. Hu, and J. L. Reno, Two-well terahertz quantum cascade lasers with suppressed carrier leakage, Appl. Phys. Lett. **111**, 111107 (2017).

[14] S. Liu, X. Yuan, W. Fu, Y. Yan, Y. Zhang, H. Li, and R. Zhong, The coaxial gyrotron with two electron beams. I. Linear theory and nonlinear theory, Phys. Plasmas **14**, 103113 (2007).

[15] S. Liu, X. Yuan, D. Liu, Y. Yan, Y. Zhang, H. Li, and R. Zhong, The coaxial gyrotron with two electron beams. II. Dual frequency operation, Phys. Plasmas **14**, 103114 (2007).

[16] R. W. Sanders, V. Jaccarino, and S. M. Rezende, Magnetic polariton, impurity mode enhancement, and superradiance effects in FeF_2, Solid State Commun. **28**, 907 (1978).

[17] J. Torrejon, M. Riou, F. A. Araujo, S. Tsunegi, G. Khalsa, D. Querlioz, P. Bortolotti, V. Cros, K. Yakushiji, A. Fukushima, H. Kubota, S. Yuasa, M. D. Stiles, and J. Grollier, Neuromorphic computing with nanoscale spintronic oscillators, Nature **547**, 428 (2017).

[18] V. Baltz, A. Manchon, M. Tsoi, T. Moriyama, T. Ono, and Y. Tserkovnyak, Antiferromagnetic spintronics, Rev. Mod. Phys. **90**, 015005 (2018).

[19] J. Sinova, S. O. Valenzuela, J. Wunderlich, C. H. Back, and T. Jungwirth, Spin Hall effects, Rev. Mod. Phys. **87**, 1213 (2015).

[20] T. Kampfrath, M. Battiato, P. Maldonado, G. Eilers, J. Notzold, S. Mahrlein, V. Zbarsky, F. Freimuth, Y. Mokrousov, S. Blugel, M. Wolf, I. Radu, P. M. Oppeneer, and M. Munzenberg, Terahertz spin current pulses controlled by magnetic heterostructures, Nat. Nanotechnol. **8**, 256 (2013).

[21] G. Torosyan, S. Keller, L. Scheuer, R. Beigang, and E.Th. Papaioannou, Optimized spintronic terahertz emitters based on epitaxial grown Fe/Pt layer structures, Sci. Rep. **8**, 1311 (2018).

[22] D. Yue, W. Lin, J. Li, X. Jin, and C. L. Chien, Spin-to-Charge Conversion in Bi Films and Bi/Ag Bilayers, Phys. Rev. Lett. **121**, 037201 (2018).

[23] T. Seifert *et al.*, Efficient metallic spintronic emitters of ultrabroadband terahertz radiation, Nat. Photo. **10**, 483 (2016).

[24] Y. Wu, M. Elyasi, X. Qiu, M. Chen, Y. Liu, L. Ke, and H. Yang, High-performance THz emitters based on ferromagnetic/nonmagnetic heterostructures, Adv. Mater. **29**, 1603031 (2017).

[25] T. S. Seifert, N. M. Tran, O. Gueckstock, S. M. Rouzegar, L. Nadvornik, S. Jaiswal, G. Jakob, V. V. Temnov, M. Münzenberg, M. Wolf, M. Kläui, and T. Kampfrath, Terahertz spectroscopy for all-optical spintronic characterization of the spin-Hall-effect metals Pt, W and $Cu_{80}Ir_{20}$, J. Phys. D: Appl. Phys. **51**, 364003 (2018).

[26] T. Seifert, S. Jaiswal, M. Sajadi, G. Jakob, S. Winnerl, M. Wolf, M. Klaui, and T. Kampfrath, Ultrabroadband single-cycle terahertz pulses with peak fields of 300 kV cm-1 from a metallic spintronic emitter, Appl. Phys. Lett. **110**, 252402 (2017).

[27] T. T. Ong and N. Nagaosa, Spin Transport and Accumulation in a 2D Weyl Fermion System, Phys. Rev. Lett. **121**, 066603 (2018).

[28] P. M. Oppeneer and A. Liebsch, Ultrafast demagnetization in Ni: Theory of magneto-optics for non-equilibrium electron distributions, J. Phys. Condens. Matter **16**, 5519 (2004).

[29] C. Stamm, T. Kachel, N. Pontius, R. Mitzner, T. Quast, K. Holldack, S. Khan, C. Lupulescu, E. F. Aziz, M. Wietstruk, H. A. Durr, and W. Eberhardt, Femtosecond modification of electron localization and transfer of angular momentum in nickel, Nat. Mater. **6**, 740 (2007).

[30] A. Melnikov, I. Razdolski, T. O. Wehling, E.Th. Papaioannou, V. Roddatis, P. Fumagalli, O. Aktsipetrov, A. I. Lichtenstein, and U. Bovensiepen, Ultrafast Transport of Laser-Excited Spin-Polarized Carriers in Au/Fe/MgO (001), Phys. Rev. Lett. **107**, 076601 (2011).

[31] M. Battiato, K. Carva, and P. M. Oppeneer, Super-Diffusive Spin-Transport as a Mechanism of Ultrafast Demagnetization, Phys. Rev. Lett. **105**, 027203 (2010).

[32] V. P. Zhukov, E. V. Chulkov, and P. M. Echenique, Lifetimes and inelastic mean free path of low-energy excited electrons in Fe, Ni, Pt, and Au: Ab initio GW+T calculations, Phys. Rev. B **73**, 125105 (2006).

[33] K. Ando, S. Takahashi, J. Ieda, Y. Kajiwara, H. Nakayama, T. Yoshino, K. Harii, Y. Fujikawa, M. Matsuo, S. Maekawa, and E. Saitoh, Inverse spin-Hall effect induced by spin pumping in metallic system, Appl. Phys. Lett. **109**, 103913 (2011).

[34] S. Liu, P. Zhang, W. Liu, S. Gong, R. Zhong, Y. Zhang, and M. Hu, Surface Polariton Cherenkov Light Radiation Source, Phys. Rev. Lett. **109**, 153902 (2012).

[35] M. Battiato, K. Carva, and P. M. Oppeneer, Theory of laser-induced ultrafast superdiffusive spin transport in layered heterostructures, Phys. Rev. B **86**, 024404 (2012).

[36] J. J. Xu, X. Jiang, H. C. Zhang, J. Wang, S. Qu, and T. J. Cui, Diffraction radiation based on an anti-symmetry structure of spoof surface-plasmon waveguide, Appl. Phys. Lett. **110**, 021118 (2017).

[37] A. Okajima and T. Matsui, Electron-beam induced terahertz radiation from graded metallic grating, Opt. Exp. **22**, 17490 (2014).

[38] S. Liu, M. Hu, Y. Zhang, Y. Li, and R. Zhong, Electromagnetic diffraction radiation of a subwavelength-hole array excited by an electron beam, Phys. Rev. E **80**, 036603 (2009).

[39] A. Kianinejad, Z. N. Chen, and C.-W. Qiu, A single-layered spoof-plasmon-mode leaky wave antenna with consistent gain, IEEE Trans. Antenn. Propag. **65**, 681 (2017).

[40] F. Liu, L. Xiao, Y. Ye, M. Wang, K. Cui, X. Feng, W. Zhang, and Y. Huang, Integrated Cherenkov radiation emitter eliminating the electron velocity threshold, Nat. Photo. **11**, 289 (2018).

[41] Y. Yang, A. Massuda, C. Roques-Carmes, S. E. Kooi, T. Christensen, S. G. Johnson, J. D. Joannopoulos, O. D. Miller, I. Kaminer, and M. Soljačić, Maximal spontaneous photon emission and energy loss from free electrons, Nat. Phys. **14**, 894 (2018).

[42] M. A. Ordal, L. L. Long, R. J. Bell, S. E. Bell, R. R. Bell, R. W. Alexander, Jr., and C. A. Ward, Optical properties of the metals Al, Co, Cu, Au, Fe, Pb, Ni, Pd, Pt, Ag, Ti, and W in the infrared and far infrared, Appl. Opt. **22**, 1099 (1983).

[43] M. Weinfeld and A. Bouchoule, Electron gun for generation of subnanosecond electron packets at very high repetition rate, Rev. Sci. Intrum. **47**, 412 (1976).

[44] F. Sannibale, D. Filippetto, M. Johnson, D. Li, T. Luo, C. Mitchell, J. Staples, S. Virostek, R. Wells, and J. M. Byrd, Upgrade possibilities for continuous wave rf electron guns based on room-temperature very high frequency technology, Phys. Rev. Spec. Top. – AC **20**, 113402 (2017).

[45] W. R. Huang, E. A. Nanni, K. Ravi, K. H. Hong, A. Fallahi, L. J. Wong, P. D. Keathley, L. E. Zapata, and F. X. Kartner, Toward a terahertz-driven electron gun, Sci. Rep. **5**, 14899 (2015).

[46] Y. M. Shin, J. F. Zhao, L. R. Barnett, and N. C. Luhmann, Investigation of terahertz sheet beam traveling wave tube amplifier with nanocomposite cathode, Phys. Plasmas **17**, 123105 (2010).